Strain and composition effects on Raman vibrational modes of silicon-germanium-tin ternary alloys

J.-H. Fournier-Lupien, S. Mukherjee, S. Wirths, E. Pippel, N. Hayazawa, G. Mussler, J. M. Hartmann, P. Desjardins, D. Buca, and O. Moutanabbir

Citation: Applied Physics Letters **103**, 263103 (2013); doi: 10.1063/1.4855436
View online: http://dx.doi.org/10.1063/1.4855436
View Table of Contents: http://scitation.aip.org/content/aip/journal/apl/103/26?ver=pdfcov
Published by the AIP Publishing

Strain and composition effects on Raman vibrational modes of silicon-germanium-tin ternary alloys

J.-H. Fournier-Lupien,[1] S. Mukherjee,[1] S. Wirths,[2] E. Pippel,[3] N. Hayazawa,[1,a)] G. Mussler,[2] J. M. Hartmann,[4] P. Desjardins,[1] D. Buca,[2] and O. Moutanabbir[1,b)]
[1]*Department of Engineering Physics, École Polytechnique de Montréal, Montréal, C. P. 6079, Succ. Centre-Ville, Montréal, Québec H3C 3A7, Canada*
[2]*Peter Grünberg Institute 9 and JARA-FIT, Forschungszentrum Juelich, 52425 Juelich, Germany*
[3]*Max Planck Institute of Microstructure Physics, Weinberg 2, Halle (Saale) 06120, Germany*
[4]*CEA, LETI, Minatec Campus, 17 rue des Martyrs, 38054 Grenoble, France*

(Received 4 November 2013; accepted 8 December 2013; published online 26 December 2013)

We investigated Raman vibrational modes in silicon-germanium-tin layers grown epitaxially on germanium/silicon virtual substrates using reduced pressure chemical vapor deposition. Several excitation wavelengths were utilized to accurately analyze Raman shifts in ternary layers with uniform silicon and tin content in 4–19 and 2–12 at. % ranges, respectively. The excitation using a 633 nm laser was found to be optimal leading to a clear detection and an unambiguous identification of all first order modes in the alloy. The influence of both strain and composition on these modes is discussed. The strain in the layers is evaluated from Raman shifts and reciprocal space mapping data and the obtained results are discussed in the light of recent theoretical calculations. © *2013 AIP Publishing LLC*. [http://dx.doi.org/10.1063/1.4855436]

The realization of near- and mid-infrared photonics in group-IV semiconductors will enable on-chip complementary metal-oxide-semiconductor optoelectronic systems which will create a wealth of opportunities in chemical and biological sensing, spectroscopy, and free-space communication.[1] In this perspective, silicon-germanium-tin (SiGeSn) based systems were suggested as excellent candidates for monolithic chips.[1,2] For instance, two systems were recently designed and simulated for mid-infrared lasing: a double heterostructure consisting of $Ge_{0.94}Sn_{0.06}$ and $Ge_{0.75}Si_{0.15}Sn_{0.1}$ layers[3] and a PIN-diode $Ge_{0.94}Sn_{0.06}/Ge_{0.75}Si_{0.15}Sn_{0.1}$ multi-quantum well.[2] These– multi-quantum-well structures would have to be grown on relaxed $Ge_{0.75}Si_{0.15}Sn_{0.1}$ buffer on Si or SOI (silicon-on-insulator). Implementing the proposed SiGeSn-based devices remains, however, a formidable challenge from materials perspective due to the low solubility (<1 at. %) of Sn in Si and Ge. The recent progress in low-temperature chemical vapor deposition (CVD) alleviates some of these difficulties.[4–7] Using conventional precursors, the fabrication of device quality $Ge_{1-y}Sn_y$ binary alloys with high Sn fraction ($y < 0.15$) and $Si_xGe_{1-x-y}Sn_y$ ternary alloys ($y = 2\%–12\%$) was recently demonstrated.[4–6] Note, however, that GeSn attracted a great deal of attention for more than two decades ago as a potential direct band gap material (see Ref. 8 and references therein), but its thermodynamic instabilities prevented its use in reliable devices for large scale industrial applications. In contrast, recent theoretical investigations suggested that Sn-based ternary alloys are relatively stable due to the mixing entropy.[4] Besides the potential applications in photonics and optoelectronics, Sn-containing group IV semiconductor alloys and heterostructures are also highly relevant for high-mobility and low-power electronics. For instance, the increase in the contribution of direct transitions was found to boost the performance of tunnel field-effect transistors.[6,9] Moreover, the control of the composition and structure of SiGeSn alloys and heterostructures are also crucial to enable carbon-free energy conversion devices such as thermoelectrics and high-efficiency multijunction solar cells.[4,7,10]

In order to develop the aforementioned technologies, it is of utmost importance to establish a deep understanding of the interplay between the composition, structure, and physical properties of SiGeSn alloys and heterostructures. Developing this body of knowledge is also critical to expand our fundamental understanding of the basic properties of metastable alloys in general. With this perspective, this letter reports on the use of multi-wavelength micro-Raman spectroscopy to characterize SiGeSn layers grown on Si(100) using high crystalline quality Ge buffer layers. The use of several wavelengths allowed a precise analysis of composition and stress at different depths within the same ultrathin layer. Moreover, employing several laser lines with wavelengths in the 532–785 nm range provides valuable insights into faint changes in vibrational modes of SiGeSn and their evolution as a function of Si, Ge, and Sn concentrations. This ability to detect subtle changes in Raman spectra at different depths enabled a more rigorous identification and discrimination of Raman vibrational modes. Additionally, the stress in these layers was also estimated from Raman and x-ray reciprocal space mapping (RSM) data and discussed in the light of recent calculations combining the empirical pseudopotential method (EPM) and band structure calculations in a surpercell.[11]

The investigated SiGeSn layers were grown using a metal cold-wall reduced pressure chemical vapor deposition AIXTRON TRICENTR® reactor (RP-CVD) for 200/300 mm

a)Permanent address: Near-field Nanophotonics Research Team, RIKEN, The Institute of Physical and Chemical Research, 2-1 Hirosawa, Wako, Saitama 351-0198, Japan.
b)Author to whom correspondence should be addressed. Electronic mail: oussama.moutanabbir@polymtl.ca.

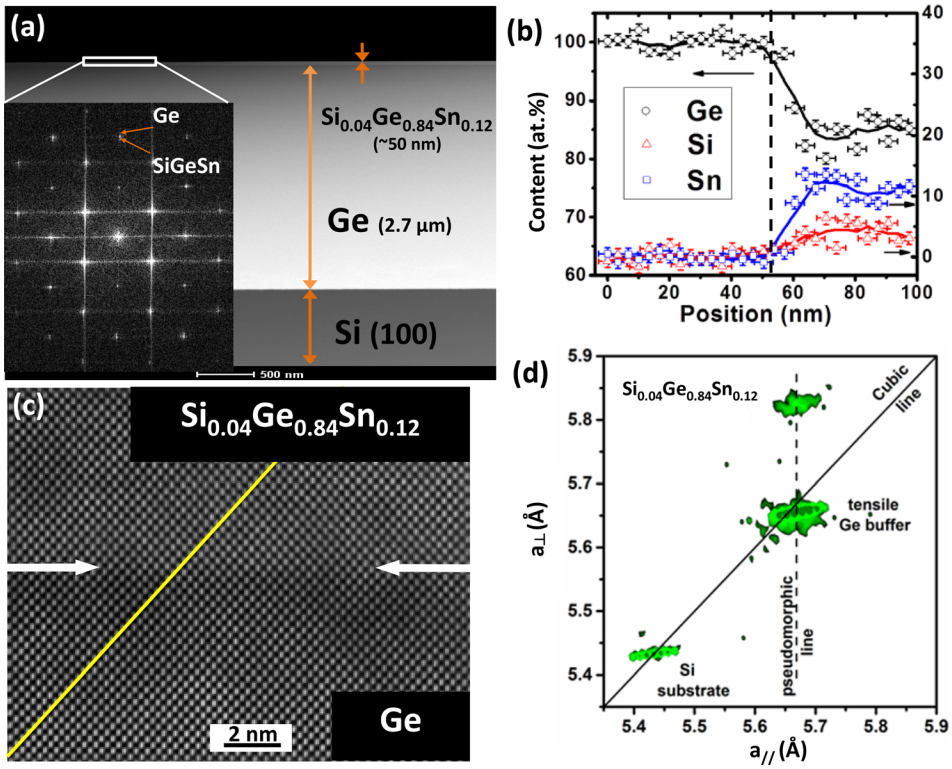

FIG. 1. (a) Low magnification HAADF/STEM image of $Si_{0.04}Ge_{0.84}Sn_{0.12}$/Ge/Si structure. The diffraction pattern measured at the SiGeSn/Ge interface is shown in the inset. (b) EDX Ge, Si, and Sn along the whole ~50 nm-thick SiGeSn layer. Solid lines correspond to local average concentrations and vertical dashed line denotes the interface. (c) High resolution TEM image of the $Si_{0.04}Ge_{0.84}Sn_{0.12}$/Ge interface. No dislocations are found at the interface; only a change on the order of 1.6% in the out-of-plane lattice parameter is observed between Ge and SiGeSn. (d) Reciprocal space map of the $Si_{0.04}Ge_{0.84}Sn_{0.12}$/Ge/Si structure around the asymmetric (224) reflection.

wafers.[6] The epitaxial layers were grown using Si_2H_6, Ge_2H_6 (10% diluted in H_2), and $SnCl_4$ precursors using N_2 as carrier gas, which warrant reasonable growth rates at temperatures in the 350–475 °C range. The growth of SiGeSn layers was performed on Si(100) wafers using low-defect density Ge virtual susbtrates.[12,13] In this research, the SiGeSn layers were grown on the virtual substrates developed in Ref. 13. The SiGeSn layers were grown at Si and Sn concentrations in the range of 4%–19% and 2%–12%, respectively. Prior to Raman investigations, the composition and structural properties of SiGeSn/Ge/Si layers were characterized using Rutherford backscattering spectrometry (RBS), RSM, and transmission electron microscopy (TEM). Backscattering micro-Raman experiment were carried out in Renishaw InVia RM 3000 instrument using three different laser lines operating at wavelengths of 532, 633, and 785 nm. The laser beam is focused on the sample surface to a spot diameter of ~1–1.3 μm. The scattered light was diffracted by an 1800 lines/mm grating and finally detected by a liquid nitrogen-cooled charge-coupled device (CCD). To avoid local heating, the laser power for the three wavelengths was kept below 5 mW. For a given sample and at a fixed laser wavelength, the recorded Raman spectra are averaged over several spots on the sample surface. TEM analyses were carried out on a selected set of samples using an aberration-corrected (C_s probe corrector) FEI TITAN 80–300 analytical scanning transmission electron microscope operating at 300 kV, which yields a spatial resolution of about 100 pm in both modes. This microscope is also equipped with an energy dispersive x-ray (EDX) detector with a detection sensitivity of about 0.5 at. %.

Fig. 1(a) displays a High Angle Annular Dark Field Scanning Transmission Electron Microscopy (HAADF/STEM) image of a ~50 nm-thick $Si_{0.04}Ge_{0.84}Sn_{0.12}$ layer grown on a 2.7 μm-thick Ge virtual substrate. The average composition was estimated from RBS spectra (not shown here), while EDX was utilized to probe the local composition. The obtained EDX profiles indicate that the composition along the whole thickness of the ternary layer is uniform (Fig. 1(b)). Fig. 1(c) exhibits a high resolution STEM image near the $Si_{0.04}Ge_{0.84}Sn_{0.12}$/Ge interface. This figure clearly indicates the absence of dislocations or extended defects in the ternary layer or at the interface. The diffraction pattern (Fig. 1(a), inset) measured at the interface SiGeSn-Ge confirms this high crystallinity as well as the absence of Sn precipitates. Also, it can be noticed that Ge and $Si_{0.04}Ge_{0.84}Sn_{0.12}$ diffraction spots are in-plane superposed and slightly departed from each other in the out-of-plane direction, as expected from coherent growth. This indicates that the two layers have the same in-plane lattice parameter but different out-of-plane parameters. This observation stands in perfect agreement with RSM data displayed in Fig. 1(d). This figure shows the RSM map around the asymmetric (224) reflection for $Si_{0.04}Ge_{0.84}Sn_{0.12}$/Ge/Si heterostructure. It is noticeable that the top layer is under compressive strain since the in-plane lattice parameter ($a_{//}$) of GeSiSn is identical to Ge lattice parameter as opposed to the out-plane lattice ($a_\perp$) which is larger in the SiGeSn layer. Since the top layer is pinned to Ge substrate, the structure of the top layer is under a tetragonal distortion.

As mentioned above, multi-wavelength micro-Raman spectroscopy was utilized to perform a detailed investigation of vibrational modes in SiGeSn and their evolution as a function of composition and strain. Fig. 2 displays representative Raman spectra recorded using the three laser lines for $Si_xGe_{1-x-y}Sn_y$/Ge/Si layers at $(x; y) = (0.2; 0.03)$ and $(0.05; 0.12)$. Depending on the composition and laser wavelength, the main Raman modes that can be observed are Sn-Sn (~190 cm^{-1}), Ge-Sn (~260 cm^{-1}), Ge-Ge (~300 cm^{-1}), Si-Ge (~390 cm^{-1}), and Si-Si (~435 cm^{-1} and ~450 cm^{-1})

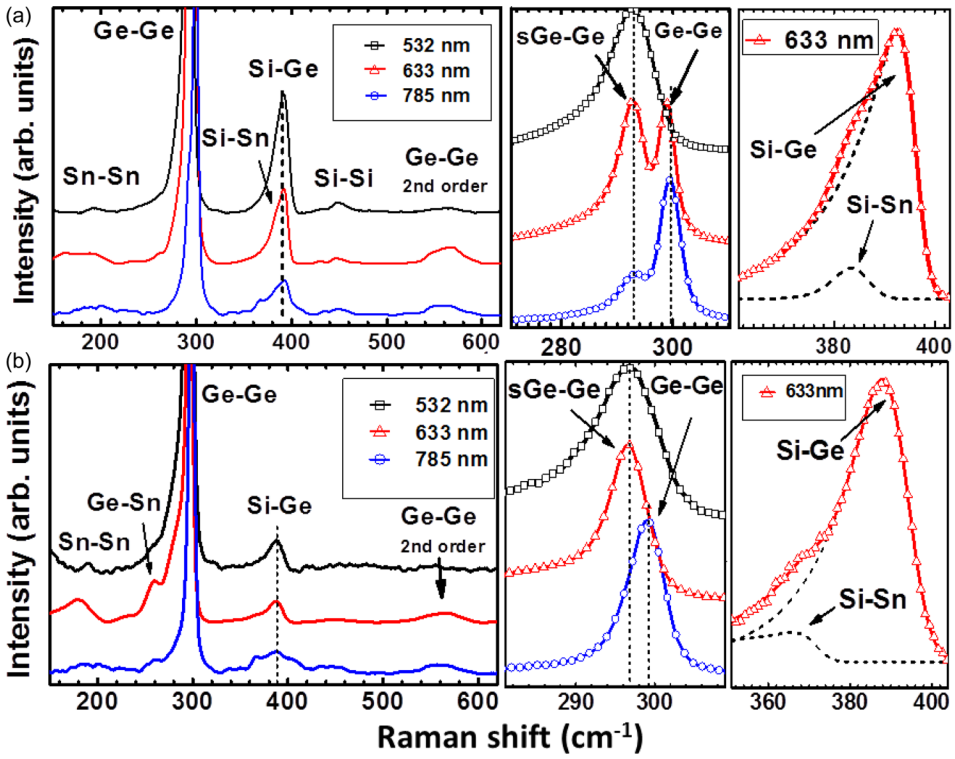

FIG. 2. Raman spectra of $Si_{0.18}Ge_{0.78}Sn_{0.04}$/Ge/Si (a) and $Si_{0.04}Ge_{0.84}Sn_{0.12}$/Ge/Si (b) samples recorded using three different laser wavelengths. The insets display the Raman spectra in the wavenumber regions around Ge-Ge and Si-Ge modes.

modes. The Si-Si modes display a strong downshift as compared to Si-Si mode in bulk Si (~520 cm^{-1}), which is attributed to Si-Si vibration in proximity of one or more Ge or Sn atoms, as previously observed in other group IV alloys.[4,14–16] It is also noteworthy that the relative intensities of these peaks are very sensitive to composition and laser wavelength. The latter defines the volume probed which can include the underlying Ge in addition to the top $Si_xGe_{1-x-y}Sn_y$. For instance, for the layer with the lowest Sn content (Fig. 2(a)), two Ge-Ge modes are observed at different wavenumbers when the measurements are carried out using 633 or 785 nm excitation. The high frequency Ge-Ge peak, centred on ~300 cm^{-1}, corresponds to the longitudinal optical (LO) phonons mode in the underlying Ge layer, whereas the low-frequency mode (~293 cm^{-1}) is Ge-Ge mode in $Si_{0.18}Ge_{0.78}Sn_{0.04}$ layer. This shift as compared to the mode in bulk Ge is attributed to the influence of both strain and composition. The individual contributions of each of these effects are addressed below. Note that the Ge-Ge peak from the underlying Ge layer vanishes when the analysis is performed using the 532 nm laser due to a much shallower penetration in $Si_xGe_{1-x-y}Sn_y$. Interestingly, this is also the case for the layer with the highest Sn content (Fig. 2(b)) even at a larger laser wavelength (633 nm). This is indicative of an enhanced light absorption in the SiGeSn (i.e., lower penetration depth) as Sn content increases. Curiously enough, at 785 nm the Ge-Ge relaxed mode emerges and becomes significantly predominant suggesting that at this wavelength, the $Si_{0.04}Ge_{0.84}Sn_{0.12}$ becomes relatively more transparent at this wavelength and light scattering occurs mainly in the underlying Ge layer. The same conclusion can be drawn from other Sn- and Si-related modes which become nearly invisible at 785 nm.

It is also important to note that by comparing the spectra recorded at different wavelengths, it appears that the excitation by the 633 nm laser enables a clear detection of all Raman modes in the ternary layers independently of their composition. This can perhaps be attributed to the fact that this wavelength might be close to resonance with the alloy's E_1 gap as suggested by D'Costa *et al.*[14] However, in that study, the growth of ternary layers on GeSn buffer prevented the excitation using a red laser due to the strong Ge-Ge and Ge-Sn background signals from the buffer layer.[14] Consequently, the authors utilized a low penetration depth excitation (514.5 nm), which is not ideal for the detection of Sn-related modes.[14,17] Herein, the direct growth on Ge alleviates this difficulty and allows the use of a 633 nm laser to excite the alloys leading to an unambiguous identification of vibrational modes in the ternary layers. Thus, it becomes possible to accurately study faint changes in the behavior Raman modes as a function of strain and composition. Thus, in the following, we focus our analysis and discussion on data obtained using the optimal 633 nm excitation.

Fig. 3 shows a selected set of Raman spectra of $Si_xGe_{1-x-y}Sn_y$/Ge layers for x and y varying in the 4–19 and 2–12 at. % ranges corresponding to a y/x ratio in the 0.11–2.75 range. Expectedly, the data indicate that Sn-Sn and Ge-Sn modes become more important as the fraction of Sn relative to Si (y/x) increases. This is also the case for the Si-Sn mode even though it is not clearly detected as it is overwhelmed by the stronger Si-Ge mode. However, a close examination of the spectra around 400 cm^{-1} indicates an asymmetric broadening near the Si-Ge peak which becomes more significant as Sn content increases (Fig. 2, insets). In order to determine the position of different vibrational modes, we fit the spectra using the exponentially modified Gaussian (EMG) function.[14,18] The obtained data are summarized in Table I. Expectedly, Raman shifts of the detected vibrational modes are sensitive to the composition of the layer. Ge-Ge vibrational mode (ω_{Ge-Ge}) in the underlying

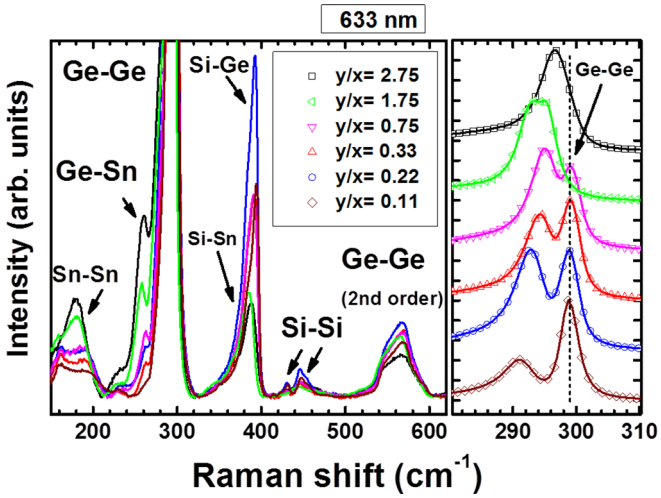

FIG. 3. (Left) Raman spectra of the $Si_xGe_{1-x-y}Sn_y$ layers at different compositions. The corresponding y/x ratio is also indicated. The spectra were recorded using the excitation wavelength of 633 nm. (Right) The same spectra shown near the Ge-Ge mode.

Ge layer is not affected by the change in the composition of the top layer, but it is slightly down shifted as compared to Ge-Ge mode in bulk Ge ($\sim$301 cm^{-1}). This shift is induced by the tensile stress in the Ge layer, which built up during the Ge deposition due to thermal mismatch between Ge and Si. The difference between Ge-Ge mode in the Ge layer and Ge-Ge mode in the ternary layers (ω_{sGe-Ge}) results from the simultaneous influence of both strain and composition. It is noticeable that ω_{sGe-Ge} shifts up as y/x increases. Conversely, Ge-Sn and Si-Ge modes down shift for $y/x \leq 1.75$ and increase slightly for the alloy with the highest y/x ratio. Note that ω_{Ge-Sn} vanishes completely when Sn concentration is very low (2%). Similarly, the weak Si-Si vibrational mode is absent at low Si concentration ($\leq$4%) whereas the strong mode persists.

In order to address the interplay between composition and strain and evaluate the latter in ternary layers, we introduce, based on the analysis in Ref. 14, the following set of equations relating the three modes Ge-Ge, Si-Si, and Si-Ge to strain and composition

$$\begin{cases} \omega_{Ge-Ge} = \omega_0^{Ge} - a_{Ge-Ge}^{GeSi} x - a_{Ge-Ge}^{GeSn} y + b_{Ge-Ge}\varepsilon \\ \omega_{Si-Si} = \omega_0^{Si} - a_{Si-Si}^{GeSi}(1-x-y) - a_{Si-Si}^{SiSn} y + b_{Si-Si}\varepsilon \\ \omega_{Si-Ge} = \omega_{0,Si-Ge}^{GeSi}(x,y) + a_{Si-Ge} y + b_{Si-Ge}\varepsilon, \end{cases} \quad (1)$$

where $\omega_0^{Ge} = 301\,cm^{-1}$ and $\omega_0^{Si} = 520\,cm^{-1}$ correspond to Raman shits of Ge-Ge and Si-Si modes in bulk Ge and Si, respectively. ε is the in-plane strain and a, b are linear coefficients associated with composition and strain, respectively. Herein, we used the following b parameters:[19–21] $b_{Ge-Ge} = -415\,cm^{-1}$, $b_{Si-Si} = -984\,cm^{-1}$, and $b_{Si-Ge} = -575\,cm^{-1}$. The parameter $\omega_{0,Si-Ge}^{GeSi}(x,y)$, the position of Si-Ge peak in SiGe alloy, is given by an empirical polynomial expression reported by Shin *et al.*[22] The parameters a are estimated by fitting our experimental data. For this, we first extracted lattice parameters from RSM data and then estimated the corresponding strain in the ternary layers (Table II). Assuming a tetragonal distortion of the lattice, the lattice parameter is expressed as $a_{0,exp} = \frac{a_\perp + \frac{2C_{12}}{C_{11}} a_{//}}{\frac{2C_{12}}{C_{11}} + 1}$, where C_{11} and C_{12} are the elastic constants of SiGeSn alloy linearly extrapolated from Ge, Si, and α-Sn. Additionally, we also calculated the lattice parameters of the investigated ternary layers using the expression obtained from EPM[11] studies (Table II). For the sake of comparison, lattice parameters are also calculated using Vegard's law. As a general trend, lattice parameters as measured by RSM are in good agreement with both Vergard's law and EPM. However, the latter seems to be a better approximation when the relative amount of Sn is high ($y/x = 2.75$ and 1.75).

Subsequently, the in-plane strain is calculated using lattice parameters ($a_{0,RSM}$) extracted from the RSM measurements using the following equation: $\varepsilon_{RSM} = \frac{a_{//} - a_{0,RSM}}{a_{0,RSM}}$.

TABLE I. Peak positions of different Raman modes of SiGeSn layers extracted from the spectra recorded using the 633 nm laser.

x (%)	y (%)	ω_{Ge-Sn} (cm^{-1})	ω_{sGe-Ge} (cm^{-1})	ω_{Ge-Ge} (cm^{-1})	ω_{Si-Sn} (cm^{-1})	ω_{Si-Ge} (cm^{-1})	ω_{Si-Si} (cm^{-1}) (weak)	ω_{Si-Si} (cm^{-1}) (strong)
12	4	263.0	294.2	299.0	383.7	392.0	430.3	445.7
18	4	262.7	292.7	298.9	383.5	392.6	430.4	446.5
4	11	260.1	296.8	N.A.	365.6	387.9	N.A.	449.6
8	6	260.5	294.9	299.1	383.6	391.1	430.7	447.1
19	2	N.A.	291.3	299.0	383.7	394.3	430.8	447.9
4	7	257.8	294.1	N.A.	387.3	385.1	N.A.	445.0

TABLE II. The in-plane strain in the grown SiGeSn layers obtained from x-ray data compared to the calculated values using EPM and SE models. The composition was measured using RBS. In-plane lattice and out-of-plane lattice parameters are obtained from RSM analyses.

y/x	Thickness (nm)	Growth temperature (°C)	$a_{//}$ (Å)	$a_\perp$ (Å)	$a_{0,RSM}$ (Å)	$a_{0,Vegard}$ (Å)	$a_{0,EPM}$ (Å)	ε_{RSM} (%)	ε_{SE} (%)
0.33	45	425	5.661	5.652	5.656	5.664	5.667	0.09	−0.11
0.22	65	450	5.668	5.629	5.646	5.650	5.653	0.39	0.27
2.75	53	350	5.668	5.826	5.758	5.740	5.755	−1.56	−1.52
0.75	54	400	5.665	5.709	5.690	5.689	5.697	−0.44	−0.56
0.11	57	475	5.662	5.607	5.631	5.631	5.630	0.56	0.56
1.75	40	375	5.660	5.756	5.715	5.707	5.717	−0.96	−0.99

TABLE III. Composition and strain obtained from Raman data by solving the set of equations (1) as described in the text. Also shown are the composition and strain measured by RBS and RSM, respectively.

RBS/RSM			Raman		
x (%)	y (%)	ε_{RSM} (%)	x (%)	y (%)	ε (%)
12	4	0.09	13	4	0.20
18	4	0.39	16	4	0.32
4	11	−1.56	3	11	−1.68
8	6	−0.44	11	6	−0.34
19	2	0.56	21	3	0.67

Moreover, based on lattice parameter calculations ($a_{0,EPM}$) reported in Ref. 11, we also introduce a semi-empirical (SE) model to calculate the strain $\varepsilon_{SE} = \frac{a_{//} - a_{0,EPM}}{a_{0,EPM}}$. Table II summaries the results obtained from RSM experiments and SE model. A perfect agreement between the two methods is observed for some alloys ($y/x = 2.75$, 1.75, and 0.11), but for others, EPM calculations seem to slightly overestimate the lattice parameter thus leading to lower strain values. As anticipated, the residual strain is sensitive to both Si and Sn composition. As a general trend, we observed that strain decreases (i.e., the ternary layer becomes under an increasing compression) as y/x ratio increases and roughly varies as $\varepsilon \approx 1 - 1.56 \times (y/x)^{0.5}$ for $0.1 \leq y/x \leq 2.75$. From this trend, a fully relaxed ternary layer should correspond to $y/x \sim 0.35$.

To estimate strain and composition from Raman spectra, the above set of equations (1) needs to be solved. Towards this end, we obtained the parameters a by fitting the evolution of Raman peak positions using the following expression: $f(x,y) = \omega^{GeSiSn}_{Ge-Ge} - \omega^{Ge}_{0} - b_{Ge-Ge}\varepsilon_{RSM} = -a^{GeSi}_{Ge-Ge}x - a^{GeSn}_{Ge-Ge}y$ to estimate a^{GeSi}_{Ge-Ge} and a^{GeSn}_{Ge-Ge} parameters. The fit gives $a^{GeSi}_{Ge-Ge} = 19.2\,\mathrm{cm}^{-1}$ and $a^{GeSn}_{Ge-Ge} = 93.5\,\mathrm{cm}^{-1}$. We also extended the fit to Si-Si and Si-Ge modes and obtained $a^{GeSi}_{Si-Si} = 80\,\mathrm{cm}^{-1}$, $a^{SiSn}_{Si-Si} = 160\,\mathrm{cm}^{-1}$, and $a_{Si-Ge} = 166\,\mathrm{cm}^{-1}$. Thus, the composition and strain can be directly evaluated from the measured ω_{Ge-Ge}, ω_{Si-Si}, and ω_{Si-Ge}, see Table III. This table compares Raman data to RBS (composition) and RSM (strain) data. It is noteworthy that strain and composition of different ternary layers estimated from Raman data agree reasonably well with the combined RBS and RSM data sets. Therefore, the above analysis confirms that Raman spectroscopy can be utilized for a straightforward and accurate characterization of strain and composition in SiGeSn ternary layers.

In summary, we have investigated the behavior of Raman vibrational modes in SiGeSn layers grown on Ge virtual substrates using reduced pressure chemical vapor deposition. The use of several excitations was effective to accurately analyze Raman modes in ternary layers with uniform Si and Sn content in 4–19 and 2–12 at. % ranges, respectively. Particularly, by using a 633 nm laser excitation, it becomes possible to detect all first order vibrational modes. The influence of both strain and composition on these modes was addressed and discussed based on RSM data and recent theoretical calculations. Finally, we demonstrated that Raman spectroscopy can be utilized to accurately estimate both strain and composition in SiGeSn ternary layers.

O.M. acknowledges funding from NSERC-Canada (Discovery Grants), Canada Research Chair, and Fondation de l'École Polytechnique de Montréal.

[1]R. Soref, Nat. Photonics **4**, 495 (2010).
[2]G. Sun, R. A. Soref, and H. H. Cheng, Opt. Express **18**, 19957 (2010).
[3]G. Sun, R. A. Soref, and H. H. Cheng, J. Appl. Phys. **108**, 033107 (2010).
[4]J. Xie, A. V. G. Chizmeshya, J. Tolle, V. R. D'Costa, J. Menendez, and J. Kouvetakis, Chem. Mater. **22**, 3779 (2010).
[5]V. D'Costa, Y.-Y. Fang, J. Tolle, J. Kouvetakis, and J. Menéndez, Phys. Rev. Lett. **102**, 107403 (2009).
[6]S. Wirths, A. T. Tiedemann, Z. Ikonic, P. Harrison, B. Hollaünder, T. Stoica, G. Mussler, M. Myronov, J. M. Hartmann, D. Grützmacher, D. Buca, and S. Mantl, Appl. Phys. Lett. **102**, 192103 (2013).
[7]R. T. Beeler, C. Xu, D. J. Smith, G. Grzybowski, J. Menéndez, and J. Kouvetakis, Appl. Phys. Lett. **101**, 221111 (2012).
[8]E. Kasper, J. Werner, M. Oehme, S. Escoubas, N. Burle, and J. Schulz, Thin Solid Films **520**, 3195 (2012).
[9]W. G. Vandenberghe, B. Sorée, W. Magnus, G. Groeseneken, and M. V. Fischetti, Appl. Phys. Lett. **98**, 143503 (2011).
[10]Y.-Y. Fang, J. Xie, J. Tolle, R. Roucka, V. R. D'Costa, A. V. G. Chizmeshya, J. Menendez, and J. Kouvetakis, J. Am. Chem. Soc. **130**, 16095 (2008).
[11]P. Moontragoon, R. A. Soref, and Z. Ikonic, J. Appl. Phys. **112**, 073106 (2012).
[12]V. A. Shah, A. Dobbie, M. Myronov, and D. R. Leadley, Solid-State Electron. **62**, 189 (2011).
[13]J. M. Hartmann, A. Abbadie, N. Cherkashin, H. Grampeix, and L. Clavelier, Semicond. Sci. Technol. **24**, 055002 (2009).
[14]V. D'Costa, J. Tolle, C. Poweleit, J. Kouvetakis, and J. Menéndez, Phys. Rev. B **76**, 035211 (2007).
[15]M. Bauer, C. Ritter, P. A. Crozier, J. Ren, J. Menendez, G. Wolf, and J. Kouvetakis, Appl. Phys. Lett. **83**, 2163 (2003).
[16]S. Stefanov, J. C. Conde, A. Benedetti, C. Serra, J. Werner, M. Oehme, J. Schulze, D. Buca, B. Holländer, S. Mantl, and S. Chiussi, Appl. Phys. Lett. **100**, 204102 (2012).
[17]S. Bagchi, C. D. Poweleit, R. T. Beeler, J. Kouvetakis, and J. Menéndez, Phys. Rev. B **84**, 193201 (2011).
[18]D. Lockwood and Z. Wasilewski, Phys. Rev. B **70**, 155202 (2004).
[19]F. Cerdeira, C. J. Buchenauer, F. H. Pollak, and M. Cardona, Phys. Rev. B **5**, 580 (1972).
[20]J. C. Tsang, P. M. Mooney, F. Dacol, and J. O. Chu, J. Appl. Phys. **75**, 8098 (1994).
[21]M. Stoehr, D. Aubel, S. Juillaguet, J. Bischoff, L. Kubler, D. Bolmont, F. Hamdani, B. Fraisse, and R. Fourcade, Phys. Rev. B **53**, 6923 (1996).
[22]H. K. Shin, D. J. Lockwood, and J.-M. Baribeau, Solid State Commun. **114**, 505 (2000).